An Experimental/Numerical Study on the Interfacial Damage of Bonded Joints for Fibre-Reinforced Polymer Profiles at Service Conditions

Agostina Orefice, Geminiano Mancusi, Serge Dumont, Frédéric Lebon

technologies

MDPI

Article

An Experimental/Numerical Study on the Interfacial Damage of Bonded Joints for Fibre-Reinforced Polymer Profiles at Service Conditions

Agostina Orefice [1], Geminiano Mancusi [1], Serge Dumont [2] and Frédéric Lebon [3,*]

1 Department of Civil Engineering, University of Salerno, 84084 Salerno, Italy; aorefice@unisa.it (A.O.); g.mancusi@unisa.it (G.M.)
2 Institut Montpelliérain Alexander Grothendieck, University of Nîmes, 30000 Nîmes, France; serge.dumont@unimes.fr
3 Laboratoire de Mécanique et d'Acoustique, Aix-Marseille Université, CNRS, Centrale Marseille, 13453 Marseille Cedex 13, France
* Correspondence: lebon@lma.cnrs-mrs.fr; Tel.: +33-484-524-222

Academic Editor: Manoj Gupta
Received: 3 February 2016; Accepted: 5 July 2016; Published: 12 July 2016

Abstract: In this paper a study on double lap joints made of glass fibre-reinforced polymer (GFRP) adherents and an epoxy resin as a glue is performed. Both an experimental procedure and a theoretical model with an associated numerical discretization are presented. Experimental and numerical results are discussed and compared. They indicate the possibility of performing an advanced mechanical analysis of adhesive joints based on a preliminary characterization of a few mechanical parameters.

Keywords: fibre-reinforced polymers (FRPs); interface model; double lap-joint

1. Introduction

Composite profiles are commonly used for civil engineering structures where, due to a relatively higher cost, carbon fibre-reinforced profiles (CFRPs) are still a few parts of the whole, while glass fibre-reinforced profiles (GFRPs) are, at the moment, the standard solution, especially for new innovative constructions and large scale applications. Within this context (i.e., innovative civil structures entirely made of composite materials), the safety and reliability of the adhesive bonding is still a field of investigation open to both theoretical-numerical and experimental contributions [1–6]. A recent study about adhesive bonded joints loaded in traction [7] focuses, in a general manner, on the interfacial damage which is affected by many factors, such as the thickness and width of the adherent, the number of lap surfaces, and the scarf angle (for scarf lap-joints).

Although they are widely used in technical practice, adhesive joints have not been properly assessed with reference to their performance for service conditions if applications of major importance are concerned, for example large truss covers, large bridge decks, or spatial frames.

It is a widespread assumption to formulate the constitutive behavior of composite materials within a linear-elastic (orthotropic) field. This is substantially true. Relevant nonlinear effects, however, emerge over the pre-buckling range of the structural response, due to many aspects, which can be briefly listed as follows:

- the non-linear axial, flexural, shear, and warping deformations, expecially when dealing with thin-walled open profiles [8–11];
- the creep behavior, especially for the GFRP members [12–14]; and
- the "lumped" damage within the bonding interfaces [15,16].

All previous factors exhibit a complex interplay which makes the formulation of "all-inclusive" predicting models very difficult, regardless of the analytical, numerical, or experimental nature of the proposed approach.

Given that the practical use of composite profiles for civil engineering applications, especially for GFRP members, is strongly affected, at service conditions, by deformability limitations [8], which implies, in general, requiring high values of stiffness, it seems appropriate to analyze the interfacial damage at service conditions regardless of the material/geometric non-linearities, which affect, instead, the failure load/the buckling limit for an higher load to stiffness ratio. In this perspective, it is also reasonable to account for the linear viscoelastic formulation of constitutive equations.

The previous considerations allow for performing the analysis of the mechanical behavior of FRP structures at service conditions within the linear field, except for the non-linear behavior of the adhesive interfaces. A detailed interface model with damage [17] has been, thereby, proposed to this scope: investigating the interfacial behavior accounting for damage over the initial range of the mechanical response, where the non-linear effects within the interface layer are the only expected ones. In this model, the adhesive is considered as a Kachanov-type material [18,19], where the constitutive equation of the interface is obtained after the homogenization of a micro-cracked material. Assuming that the thickness of the interface is sufficiently small, by using an asymptotic matched expansion, it is possible to obtain an equivalent law for an imperfect soft interface [20–23].

The numerical results are computed using a standard finite element method [24]. The nonlinear equation providing the stiffness of the interface is computed with a semi-implicit procedure.

2. Materials and Methods under Consideration

2.1. Experimental Methodology

In view of establishing a new strategy for the advanced analysis of composite-to-composite adhesive bonding which accounts for the interfacial damage, an experimental test aimed at calibrating the mechanical parameters of the interface model discussed below has been designed at the Materials and Structures Laboratory of Salerno University (Civil Engineering Department). The main experiments (two similar experiments) deal with a double-lap joint made of GFRP parts, as indicated in Figures 1 and 2 (unit length: mm).

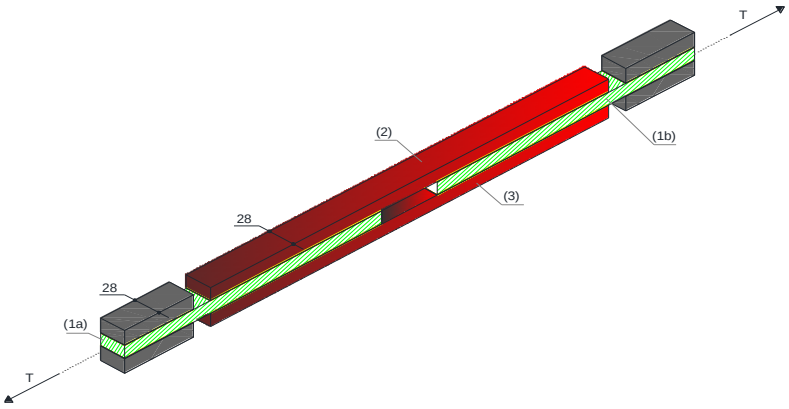

Figure 1. Joint configuration (axonometric view).

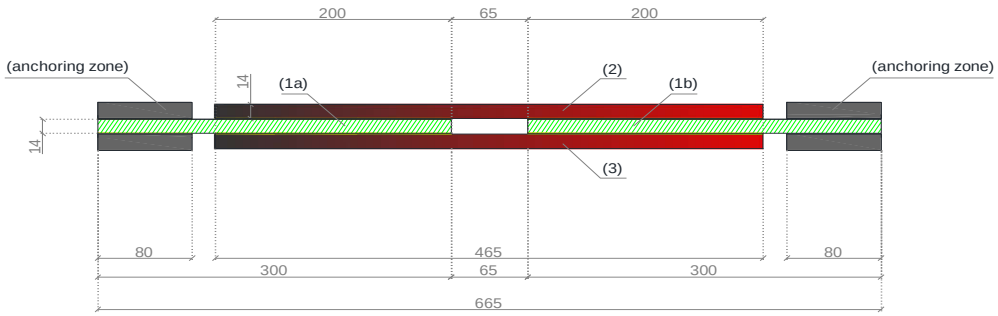

Figure 2. Joint configuration (side view).

Four adherents can be identified: "1a", "1b", "2", and "3". The cross-section is identical for all of them (28 mm × 14 mm). Each adhesive layer is 1.95 mm thick and is made of an epoxy resin. The mechanical properties of GFRP and adhesive are summarized in Tables 1 and 2.

Table 1. Mechanical properties of GFRP (from the manufacturer).

-	Value
Young's modulus	$E \geqslant 30000$ N/mm^2
Thermal expansion coefficient	$\alpha \leqslant 100 \times 10^{-6}$ K^{-1}
Tensile strength	$f_u \geqslant 700$ N/mm^2
Ultimate tensile strain	$\varepsilon_u \geqslant 1.50$ %

Table 2. Mechanical properties of Kerabuild Eco Epobond (from the manufacturer).

-	Value	Comments
Young's modulus	$E \geqslant 2000$ N/mm^2	-
Thermal expansion coefficient	$\alpha \leqslant 100 \times 10^{-6}$ K^{-1}	(-25 °C $\leqslant T \leqslant +60$ °C)
Bond strength	$\geqslant 50$ N/mm^2 $\geqslant 60$ N/mm^2 $\geqslant 70$ N/mm^2	EN 12188 (angle 50°) EN 12188 (angle 60°) EN 12188 (angle 70°)

The GFRP samples were manufactured and provided for free by ATP-Pultrusion S.r.l. (Angri, Italy), a leading company operating in the field of composite materials, whose contribution is particularly appreciated. The epoxy resin was provided for free by Kerakoll S.p.a (Sassuolo, Italy).

As a preliminary goal, two uniaxial tests have been performed on GFRP samples exhibiting the same cross-section as the adherents of the joint: 28 mm × 14 mm (Figures 3 and 4).

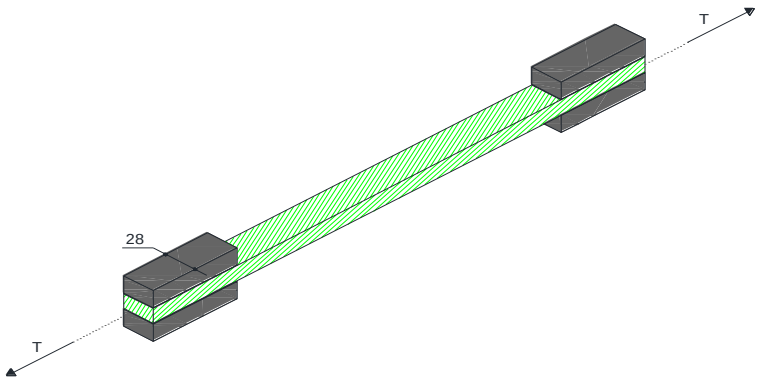

Figure 3. GFRP samples (axonometric view).

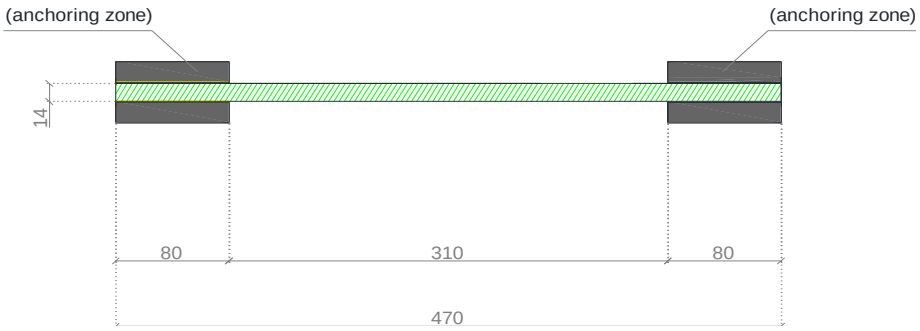

Figure 4. GFRP samples (side view).

The setup includes four metal plates bonded to both ends of the sample in order to guarantee the anchoring into the hydraulic jaws of the testing machine (Figure 5).

Figure 5. Preliminary tests on GFRP samples: Sample "1" (**left**) and Sample "2" (**right**).

The preliminary tests and the main tests have been designed in order to provoke a dominant axial stress state according to specific multi-step procedures, as indicated in Tables 3 and 4.

Table 3. Multi-step testing procedure (preliminary tests).

Cycles	-		(*)	Target	
1, 2, 3	(a)	loading	DC	+0.50	mm
	(b)	unloading	FC	0.00	N
	(c)	loading	DC	−0.50	mm
	(d)	unloading	FC	0.00	N
4, 5, 6	(a)	loading	DC	+1.00	mm
	(b)	unloading	FC	0.00	N
	(c)	loading	DC	−1.00	mm
	(d)	unloading	FC	0.00	N

(*) DC: displacement control; FC: force control.

Table 4. Multi-step testing procedure (main experiments).

Cycles			(*)	Target	
1, 2, 3	(a)	loading	DC	+1.00	mm
	(b)	unloading	FC	0.00	N
	(c)	loading	DC	0.00	mm
	(d)	unloading	FC	0.00	N
Final		loading (**)	DC	$+\infty$	mm

(*) DC: displacement control; FC: force control; (**) up to failure.

With reference to the main tests, the strain state evolution was measured by means of 12 uni-axial strain gauges with a grid size of 6.35 mm, characterized by a maximum strain capacity up to 3% and accuracy equal to 10^{-6} (Figure 6).

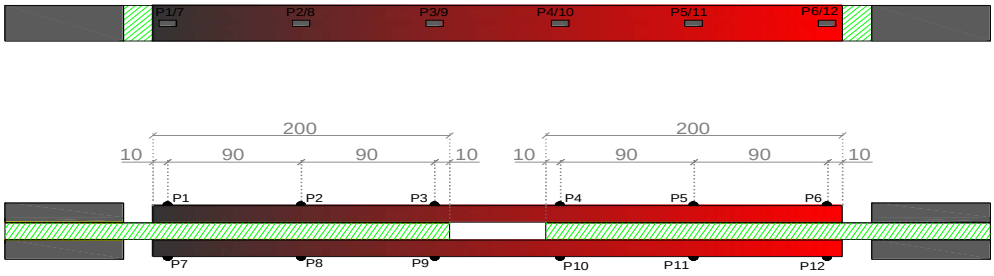

Figure 6. Strain gauge positions (bottom/top and side view).

The strain gauge reliability was ensured by an appropriate choice of adhesive and by the presence of a protective gel. As shown in Figure 6, strain gauges have been applied to the external sides of adherents "2" and "3" at defined locations. Three different cross-sections were instrumented for any interface involved in the mechanical behavior of the joint (Figures 7 and 8) Furthermore, four linear variable displacement transducers (LVDTs) were used to measure the global elongation of the joint. The experimental data were entirely acquired by means of a hardware/software system consisting of a data scanner connected to a personal computer. The scanner guarantees an automatic and modulated data acquisition, as well as a real-time adjustment of the data, due to the loss of the signal.

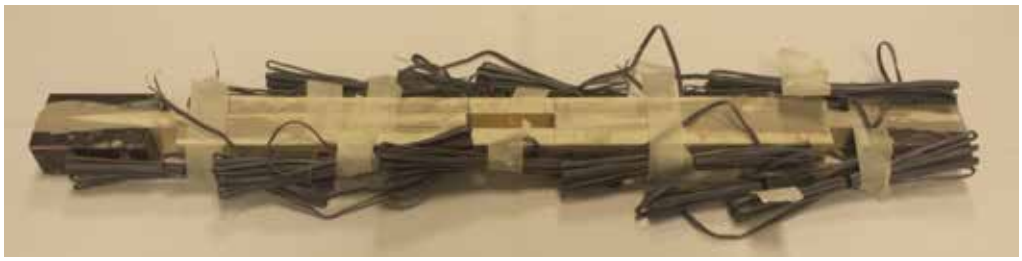

Figure 7. Joint sample "I" (after strain gauges application).

Figure 8. Joint sample "II" (after strain gauges application).

At a fixed displacement, the current axial force (T), measured by means of a load cell, depends on the stiffness of the entire system (GFRP, adhesive interfaces).

Both the preliminary tests and the main tests were carried out at constant room temperature (18 °C).

As a whole, the experiments allow the identification of the following aspects:

Via the preliminary axial tests:

- the elastic properties of the GFRP adherents (to be compared with those given by the manufacturer).

Via the main tests:

- the elastic stiffness of the joint;
- the elastic limit of the joint;
- the damage stored over any cyclic path;
- the evolution of the strains over time within the bonding length; and
- the failure load of the joint.

Although the failure load of the joint is not the actual scope of the study, it has been analyzed by means of an additional final step consisting of a monotone loading process (elongation) up to failure.

The testing equipment is presented in the following Figure 9.

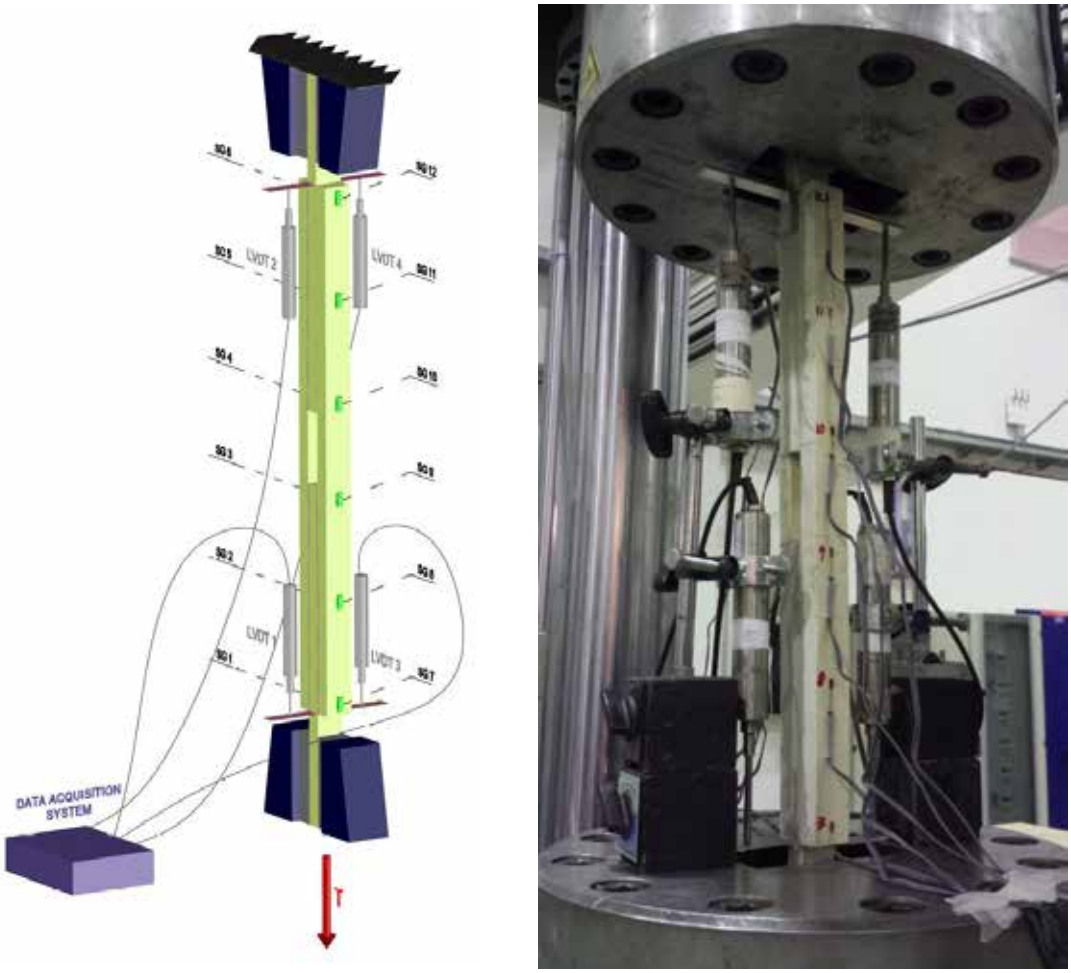

Figure 9. Main experiments. Experimental setup.

2.2. A Model of Imperfect Interface with Damage

In this section the main steps of the model of an imperfect soft interface with unilateral contact and damage evolution derived in [17] are described with the scope of comparing the experimental results with the numerical predictions.

A composite body made by two deformable solids bonded together and occupying a smooth bounded domain $\Omega \subset \mathrm{IR}^3$ is considered. An orthonormal Cartesian frame (O, e_1, e_2, e_3) is introduced and let (x_1, x_2, x_3) be taken to denote the three coordinates of a particle. The origin lies at the center of the bonding plane and the x_3-axis runs perpendicular to the bounded set S, $S = \{(x_1, x_2, x_3) \in \Omega: x_3 = 0\}$ which will be identified as the interface between the two adherents. The adherents are occupying, respectively, the domains $\Omega_\pm$ defined by $\Omega_\pm = \{(x_1, x_2, x_3) \in \Omega: \pm x_3 > 0\}$. On a part S_g of the boundary $\partial\Omega$, an external load **g** is applied, and on a part S_u of $\partial\Omega$, having a strictly positive measure such that $S_g \cap S_u = \emptyset$, the displacement is imposed to be equal to zero. Finally, a body force **f** is applied in Ω. In the following, **u** is taken to denote the displacement field, **σ** the Cauchy stress tensor and **e(u)** the strain tensor. Under the small strain hypothesis we have $e_{ij}(u) = 1/2(u_{i,j} + u_{j,i})$, where the comma stands for the partial derivative. The two adherents are supposed to be elastic, according to the following Equation (1):

$$\sigma_{ij} = a^{\pm}_{ijkl} e_{kl}(\mathbf{u}) \tag{1}$$

where $\mathbf{a}^{\pm}$ are the fourth-order elasticity tensors verifying the usual conditions of positivity and symmetry.

It is considered that the interface is made by a Kachanov-type material [18,19]. In other words, the constitutive equations are obtained after the homogenization of a micro-cracked material. The elastic coefficients of such a material, denoted by b_{ijkl}, depend on the averaged length l of these cracks, this parameter being considered as a damage parameter, and linearly on the thickness of the interface ε (the interface is soft). Usually, due to the small thickness of the interface, it is possible to use a matched asymptotic theory [20] in order to obtain an equivalent law of the imperfect soft interface [22,23]:

$$\sigma_{ij} n_j = K_{ij}(l)[u_j] \tag{2}$$

where $\mathbf{K}(l)$ is the stiffness tensor of the interface (the limit of the ratio b/ε), $\boldsymbol{n}$ the external unit vector normal to S ($\boldsymbol{n} = \mathbf{e_3}$), and $[\boldsymbol{u}]$ is the jump in the displacement across the interface S. Note that the variable l, which has the dimension of a length, can be compared with the so called "density of adhesion", which is a dimensionless variable, introduced by M. Frémond [25], which can be interpreted from a mechanical point of view as the ratio l/l_0, where l_0 is the initial crack length. For the Kachanov-type material [26], the stiffness tensor is as follows:

$$K(l) = \begin{bmatrix} \frac{L}{2Cl^2} & 0 & 0 \\ 0 & \frac{L}{2Cl^2} & 0 \\ 0 & 0 & \frac{L}{Cl^2} \end{bmatrix} \tag{3}$$

where, according to [26–28], L is the length of the interphase and C is given by:

$$C = \frac{\pi}{2} \frac{1}{\sqrt{E}} \sqrt{\frac{1}{\mu} + 2\frac{1-v}{E}} \tag{4}$$

with E, μ and v which are respectively the Young's modulus, the shear modulus and the Poisson ratio of the undamaged interface. The evolution of l is given by a simple derivation of a quadratic pseudo-potential of dissipation:

$$\gamma \dot{l} = \left(\omega - \frac{1}{2} K_{,l}(l)\, [u]_+ . [u]_+\right)_+ \tag{5}$$

where γ is a positive viscosity parameter, ω a negative parameter similar to the Dupré's energy, $()_+$ is the positive part of a value and:

$$[u]_+ = [u] \; if \; [u_3] \geqslant 0, \; [u]_+ = ([u_1], [u_2], 0) \; if \; [u_3] \leqslant 0 \tag{6}$$

It is assumed that the crack length cannot decrease and that the degradation process of the glue is irreversible. Note that it is assumed also that the crack-length variation is not active in compression. In order to avoid a possible interpenetration between the adherents, a unilateral contact law is added, $[u_3] \geqslant 0$, and the contact force is introduced which is always non positive (repulsive force):

$$\begin{cases} \sigma_{ij} n_j = K_{ij}(l)[u_j]_+ + \tau_i \\ \tau_1 = \tau_2 = 0, \; \tau_3 \leqslant 0 \, , \; \tau_3 [u_3] = 0 \end{cases} \tag{7}$$

In conclusion:

$$\begin{cases} \sigma_{ij,j} + f_i = 0 \; in \; \Omega_{\pm} \\ \sigma_{ij} n_j = g_i \; on \; S_g \\ u_i = 0 \; on \; S_u \\ \sigma_{ij} = a^{\pm}_{ijkl} e_{kl}(u) \; in \; \Omega_{\pm} \\ \sigma_{ij} n_j = K_{ij}(l) \left[u_j\right]_+ + \tau_i \; on \; S \\ \tau_1 = \tau_2 = 0, \; \tau_3 \leqslant 0, \; \tau_3 [u_3] = 0 \; on \; S \\ \gamma \dot{l} = (\omega - \frac{1}{2} K_{,l}(l) [u]_+ . [u]_+)_+ on \; S \\ l \geqslant l_0 \; on \; S \end{cases} \tag{8}$$

2.3. Numerical Modelling

In this section, a numerical procedure to solve Equation (8) is proposed. For the first five equations, a standard finite element method is used. In order to take into account the jumps in the displacements across the interface, a "flat" finite element is considered on the interface S that has all nodes on S, the first ones related to Ω_+, and the other ones related to Ω_-. It is then possible to write a stiffness matrix of this problem that is invertible and with standard error estimates (for more details, see, for example, [29]).

For the evolution of the crack length inside the interface S, a semi-implicit algorithm is developed, following the ideas discussed in [15]. First, denoted by:

$$F^2(t, l) = -\frac{1}{2} \frac{L}{Cl} K_{,l} [u]_+ . [u]_+$$

The evolution Equation (5) can be written as $\gamma \dot{l} = (\omega + \frac{Cl}{L} F^2(t, l))_+$. Then, considering a time step Δt, a discretization of the time $t^n = n\Delta t$, and denoting by l^n an approximation of $l(t^n)$, the following semi-implicit algorithm is considered:

$$\gamma \frac{l^{n+1} - l^n}{\Delta t} = (\omega + l^{n+1} \frac{C}{L} F^2(t^n, l^n))_+$$

or, equivalently:

$$l^{n+1} = max(l^n, \; \frac{l^n + \frac{\Delta t \omega}{\gamma}}{1 - \frac{C \Delta t}{L \gamma} F^2(t^n, l^n)})$$

It is important to remark that this algorithm can be improved using a fixed point procedure for the computation of $F^2(t, l)$, but this does not significantly change the numerical results presented in the next section.

3. Results

3.1. Experimental Results

As indicated above, the experimental results allow the identification of the mechanical response of both the basic material (GFRP) and the double lap joint, the latter affected by the interfacial behavior, too.

3.1.1. Preliminary Tests

The experimental results concerning two GFRP samples are presented in Tables 5 and 6. The results are shown in a sequential order according to the multi-step procedure summarized in Figures 10 and 11. It is worthy of noting that the generic step is identified by means of two points, denoted via the subscript "0" or "1", respectively indicating the start and the end point of the step. The symbol "ε" indicates the axial strain while the symbol "σ" is for the axial stress. The amount of non-reversible deformation at the end of the unloading steps (generic step "b" or "d") is also presented. Moreover, the symbol "E_{01}" indicates the Young's modulus evaluated over the generic step by means of a linear fitting of the experimental data.

Table 5. Preliminary tests (GFRP sample "1").

Cycle	Target				ε_0 [%]	ε_1 [%]	σ_0 [MPa]	σ_1 [MPa]	E_{01} [MPa]
1	loading	1.a	DC	+0.5 mm	0.000	0.161	0.00	53.14	33,642
	unloading	1.b	FC	0.0 N	0.161	0.006	53.14	0.00	33,349
	loading	1.c	DC	−0.5 mm	0.006	−0.161	0.00	−53.49	32,763
	unloading	1.d	FC	0.0 N	−0.161	−0.038	−53.49	0.00	41,828
2	loading	2.a	DC	+0.5 mm	−0.038	0.161	0.00	65.62	33,221
	unloading	2.b	FC	0.0 N	0.161	−0.030	65.62	0.00	33,173
	loading	2.c	DC	−0.5 mm	−0.030	−0.161	0.00	−42.74	32,821
	unloading	2.d	FC	0.0 N	−0.161	−0.064	−42.74	0.00	41,227
3	loading	3.a	DC	+0.5 mm	−0.064	0.162	0.00	72.79	32,515
	unloading	3.b	FC	0.0 N	0.162	−0.055	72.79	0.00	32,602
	loading	3.c	DC	−0.5 mm	−0.055	−0.161	0.00	−34.32	32,542
	unloading	3.d	FC	0.0 N	−0.161	−0.082	−34.32	0.00	41,784
4	loading	4.a	DC	+1.0 mm	−0.082	0.321	0.00	119.45	30,426
	unloading	4.b	FC	0.0 N	0.321	−0.006	119.45	0.00	32,971
	loading	4.c	DC	−1.0 mm	−0.006	−0.323	0.00	−86.32	27,121
	unloading	4.d	FC	0.0 N	−0.323	−0.119	−86.32	0.00	38,172
5	loading	5.a	DC	+1.0 mm	−0.119	0.322	0.00	115.97	26,826
	unloading	5.b	FC	0.0 N	0.322	−0.005	115.97	0.00	32,140
	loading	5.c	DC	−1.0 mm	−0.005	−0.323	0.00	−83.12	26,262
	unloading	5.d	FC	0.0 N	−0.323	−0.107	−83.12	0.00	35,486
6	loading	6.a	DC	+1.0 mm	−0.107	0.323	0.00	109.51	26,016
	unloading	6.b	FC	0.0 N	0.323	0.007	109.51	0.00	31,701
	loading	6.c	DC	−1.0 mm	0.007	−0.323	0.00	−82.81	25,243
	unloading	6.d	FC	0.0 N	−0.323	−0.098	−82.81	0.00	33,678

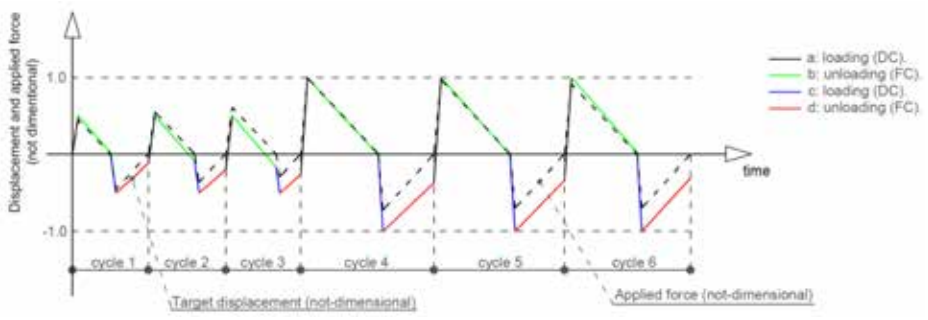

Figure 10. Multistep experimental procedure for preliminary tests (GFRP sample "1").

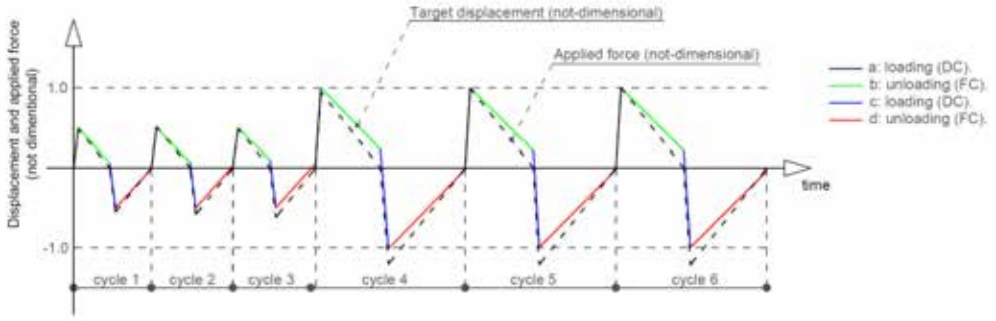

Figure 11. Multistep experimental procedure for preliminary tests (GFRP sample "2").

Table 6. Preliminary tests (GFRP sample "2").

Cycle	Target				ε_o [%]	ε_1 [%]	σ_o [MPa]	σ_1 [MPa]	E_{01} [MPa]
1	loading	1.a	DC	+0.5 mm	0.000	0.162	0.00	54.44	33,986
	unloading	1.b	FC	0.0 N	0.162	0.019	54.44	0.00	36,640
	loading	1.c	DC	−0.5 mm	0.019	−0.162	0.00	−62.66	34,932
	unloading	1.d	FC	0.0 N	−0.162	−0.004	−62.66	0.00	38,586
2	loading	2.a	DC	+0.5 mm	−0.004	0.161	0.00	57.97	35,174
	unloading	2.b	FC	0.0 N	0.161	0.021	57.97	0.00	40,150
	loading	2.c	DC	−0.5 mm	0.021	−0.162	0.00	−65.81	36,181
	unloading	2.d	FC	0.0 N	−0.162	0.008	−65.81	0.00	37,717
3	loading	3.a	DC	+0.5 mm	0.008	0.161	0.00	54.91	36,079
	unloading	3.b	FC	0.0 N	0.161	0.031	54.91	0.00	40,531
	loading	3.c	DC	−0.5 mm	0.031	−0.162	0.00	−70.15	36,721
	unloading	3.d	FC	0.0 N	−0.162	0.018	−70.15	0.00	38,001
4	loading	4.a	DC	+1.0 mm	0.018	0.323	0.00	107.01	35,550
	unloading	4.b	FC	0.0 N	0.323	0.074	107.01	0.00	41,001
	loading	4.c	DC	−1.0 mm	0.074	−0.328	0.00	−136.69	34,713
	unloading	4.d	FC	0.0 N	−0.328	−0.006	−136.69	0.00	40,143
5	loading	5.a	DC	+1.0 mm	−0.006	0.323	0.00	112.47	34,268
	unloading	5.b	FC	0.0 N	0.323	0.069	112.47	0.00	40,975
	loading	5.c	DC	−1.0 mm	0.069	−0.323	0.00	−137.65	35,248
	unloading	5.d	FC	0.0 N	−0.323	−0.007	−137.65	0.00	40,376
6	loading	6.a	DC	+1.0 mm	−0.007	0.323	0.00	112.98	34,334
	unloading	6.b	FC	0.0 N	0.323	0.069	112.98	0.00	41,424
	loading	6.c	DC	−1.0 mm	0.069	−0.323	0.00	−138.01	35,554
	unloading	6.d	FC	0.0 N	−0.323	−0.013	−138.01	0.00	40,253

In Figures 10 and 11 displacements and axial forces have been converted into non-dimensional quantities with reference to their maximum values, attained at the end of the Step 4a. The following results emerge.

For GFRP sample "1", the value of the Young's modulus (in traction) is equal to 33,084 N/mm^2 (average value over cycles 1, 2, and 3) or 30,013 N/mm^2 (average value over cycles 4, 5, and 6). The

similar values in compression are, respectively, 37,161 N/mm^2 (average value over cycles 1, 2, and 3) and 30,994 N/mm^2 (average value over cycles 4, 5, and 6).

For GFRP sample "2" the value of the Young's modulus (in traction) is equal to 37,093 N/mm^2 (average value over cycles 1, 2, and 3) or 37,925 N/mm^2 (average value over cycles 4, 5, and 6). The similar values in compression are, respectively, 37,023 N/mm^2 (average value over cycles 1, 2, and 3) and 37,715 N/mm^2 (average value over cycles 4, 5, and 6).

The previous values allow obtaining a better characterization with respect to the indication given by the manufacturer (see Table 1). This plays a pivotal role in the evaluation of the mechanical response of the joint sample.

3.1.2. Main Tests

The joint samples have been tested according to an appropriate multistep procedure up to failure, as indicated in Figures 12 and 13, where displacements and axial forces have been converted into non-dimensional quantities with reference to the values attained at the end of the Step 1a. The experimental results are presented in Tables 7 and 8.

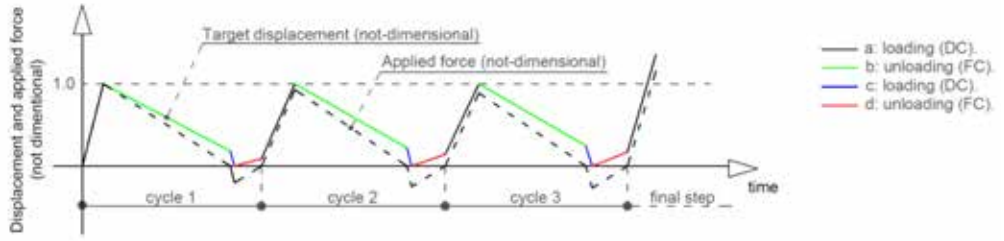

Figure 12. Multistep experimental procedure for the joint sample "I".

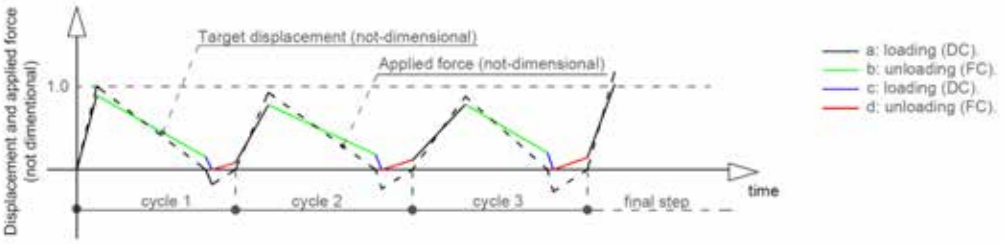

Figure 13. Multistep experimental procedure for the joint sample "II".

Table 7. Main test—joint sample "I".

Cycle	Target				T_o [kN]	T_1 [kN]	ΔL_o [mm]	ΔL_1 [mm]	K_{01}[kN/mm]
1	loading	1.a	DC	+1.0 mm	0.000	40.152	0.0000	0.9004	52.165
	unloading	1.b	FC	0.0 N	40.152	0.000	0.9004	0.1903	46.923
	loading	1.c	DC	0.0 mm	0.000	−7.728	0.1903	0.0000	47.831
	unloading	1.d	FC	0.0 N	−7.728	0.000	0.0000	0.1031	53.262
2	loading	2.a	DC	+1.0 mm	0.000	35.466	0.1031	0.9290	44.073
	unloading	2.b	FC	0.0 N	35.466	0.000	0.9290	0.2280	44.044
	loading	2.c	DC	0.0 mm	0.000	−9.482	0.2280	0.0000	49.994
	unloading	2.d	FC	0.0 N	−9.482	0.000	0.0000	0.1522	63.019
3	loading	3.a	DC	+1.0 mm	0.000	34.002	0.1522	0.9675	42.659
	unloading	3.b	FC	0.0 N	34.002	0.000	0.9675	0.2498	43.599
	loading	3.c	DC	0.0 mm	0.000	−10.142	0.2498	0.0000	46.771
	unloading	3.d	FC	0.0 N	−10.142	0.000	0.0000	0.1796	59.885
	loading	final	DC	→ +∞ mm	0.000	44.207	0.1796	1.3053	42.630

Table 8. Main test—joint sample "II".

Cycle	Target				T_o [kN]	T_1 [kN]	ΔL_o [mm]	ΔL_1 [mm]	K_{01} [kN/mm]
1	loading	1.a	DC	+1.0 mm	0.000	39.861	0.0000	0.8898	46.582
	unloading	1.b	FC	0.0 N	39.861	0.000	0.8898	0.1522	57.231
	loading	1.c	DC	0.0 mm	0.000	−7.116	0.1522	0.0000	60.699
	unloading	1.d	FC	0.0 N	−7.116	0.000	0.0000	0.0824	77.420
2	loading	2.a	DC	+1.0 mm	0.000	36.821	0.0824	0.7781	55.994
	unloading	2.b	FC	0.0 N	36.821	0.000	0.7781	0.1824	56.843
	loading	2.c	DC	0.0 mm	0.000	−9.187	0.1824	0.0000	63.129
	unloading	2.d	FC	0.0 N	−9.187	0.000	0.0000	0.1130	82.199
3	loading	3.a	DC	+1.0 mm	0.000	35.005	0.1130	0.7827	54.876
	unloading	3.b	FC	0.0 N	35.005	0.000	0.7827	0.1998	56.302
	loading	3.c	DC	0.0 mm	0.000	−10.576	0.1998	0.0000	62.529
	unloading	3.d	FC	0.0 N	−10.576	0.000	0.0000	0.1436	77.184
	loading	final	DC	→ +∞ mm	0.000	46.784	0.1436	1.0274	54.941

As for the GFRP samples, the generic step is identified by means of two points, denoted via the subscript "0" or "1". The symbol "T" denotes the axial force while the symbol "ΔL" is for the axial elongation of the joint, evaluated by means of the LVDT signals. It is important to remark that the current elongation of the joint is usually lower than the current target displacement, due to two circumstances: (i) the free elongation of the end of the sample, behind the adhesion zone; and (ii) possible sliding within the anchoring devices.

The amount of non-reversible elongation at the end of the unloading steps (generic step "b" or "d") is also presented. Finally, the symbol "K_{01}" indicates the axial stiffness of the joint, evaluated over the generic step by means of a linear fitting of the experimental data.

It is important to remark that the experimental failure loads are equal to 44,207 N or 46,784 N, respectively, for the joint samples "I" and "II". The corresponding global elongations are ΔL = 1.3053 mm and ΔL = 1.0274 mm. The post-failure configuration is shown in Figures 14 and 15.

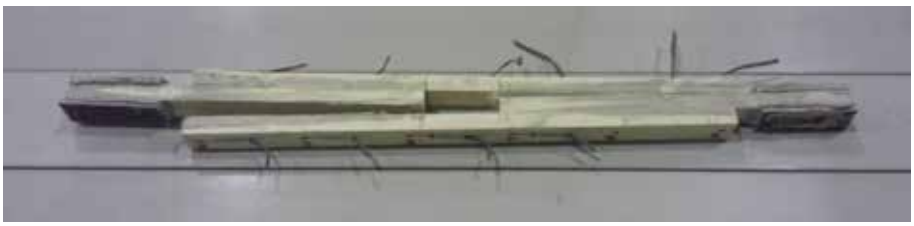

Figure 14. Post-failure configuration—joint sample "I".

Figure 15. Post-failure configuration—joint sample "II".

At collapse, two opposite adhesive interfaces simultaneously fail. Moreover, they are anti-symmetrically placed with respect to the mid-span cross-section of the joint samples.

The load versus elongation curves are presented in Figures 16 and 17.

The analysis of the strain gauge signals represents the final outcome of the experimental study. In Tables 9 and 10, the strain gradients (de_i/dT) attained within the FRP over the four adhesive interfaces are presented, with e_i being the strain returned by the electrical gauge placed at the location P_i (Figure 18) and T the applied axial force. The strain gradients presented in Tables 9 and 10 have

been averaged over the loading step "1a" (cycle 1) indicated in Table 7 (0 N < T < 40.152 kN) or Table 8 (0 N < T < 39.861 kN). Moreover, they are magnified by 1×10^6. Four additional locations have been considered (Q_i, i = 3, 4, 9, 10). They represent relevant cross-sections of the equilibrium scheme depicted in Figure 18. It is important to underline that the strain gradients at these locations come from a linear extrapolation based on the actual measurements of the neighbouring strain gauges. As an example, the strain at Q_3 has been evaluated accounting for the strains attained at P_1, P_2, and P_3. The last column shows the gradient of the axial force attained within the external adherents of the joint (adherents "2" and "3" indicated in Figure 2). They have been evaluated by means of the following relationship: EA de_i/dT, with EA denoting the axial stiffness of the GFRP adherent (EA = 37,000 N/mm^2 × 28 mm × 14 mm), estimated accounting for the experimental characterization of the Young's modulus of the GFRP explained in Section 3.1.

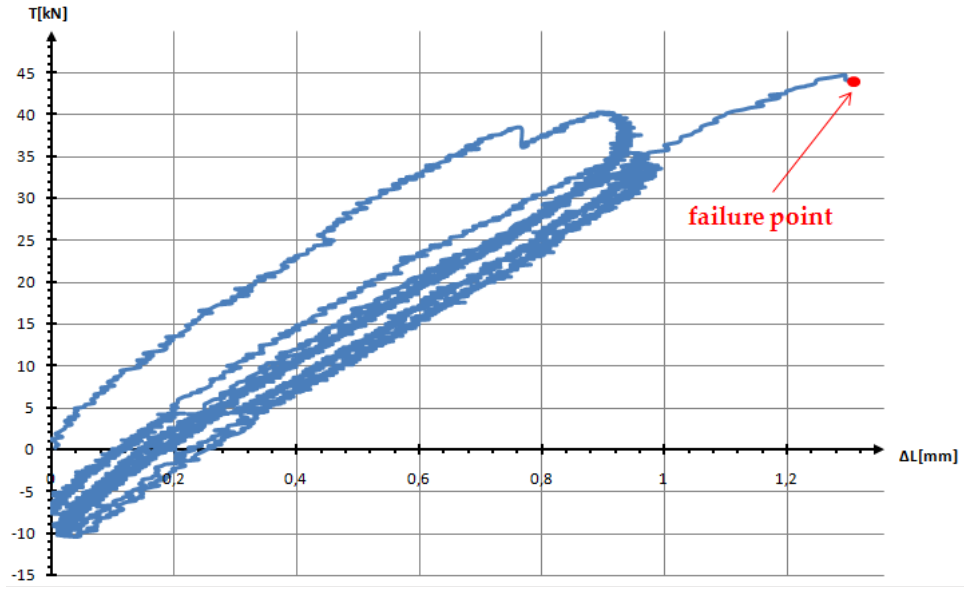

Figure 16. Load versus elongation graph—joint sample "I".

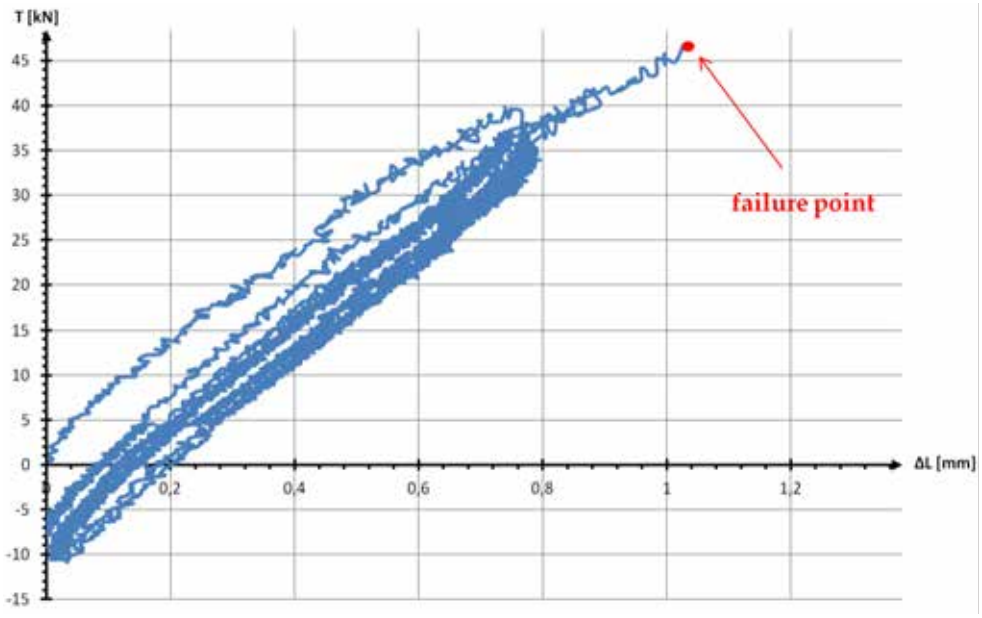

Figure 17. Load versus elongation graph—joint sample "II".

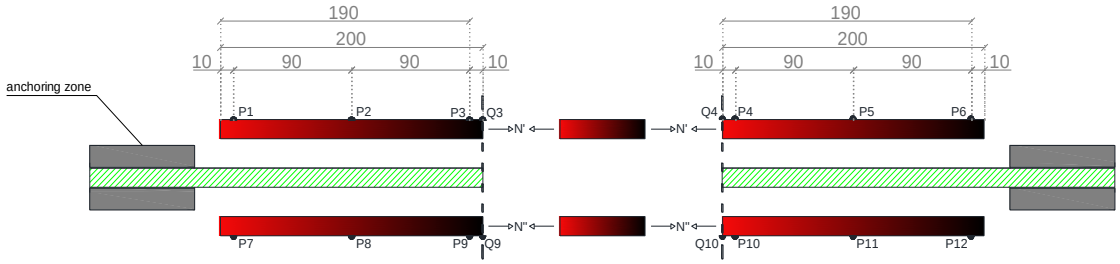

Figure 18. Strain gauges location and equilibrium scheme (unit length: mm).

Table 9. Strain and axial force gradients—joint sample "I".

Position	$\frac{de_i}{dT}$	EA $\frac{de_i}{dT}$	Position	$\frac{de_i}{dT}$	EA $\frac{de_i}{dT}$
	rad $\times 10^6/\mathrm{N}^{-1}$			rad $\times 10^6/\mathrm{N}^{-1}$	
P_1	0.0069	0.101	P_7	0.0012	0.017
P_2	0.0208	0.302	P_8	0.0120	0.174
P_3	0.0347	0.504	P_9	0.0228	0.330
Q_3	0.0363	0.526	Q_9	0.0240	0.347
Q_4	0.0334	0.485	Q_{10}	0.0265	0.384
P_4	0.0320	0.464	P_{10}	0.0253	0.366
P_5	0.0188	0.272	P_{11}	0.0109	0.159
P_6	0.0055	0.080	P_{12}	0.0034	0.050

Table 10. Strain and axial force gradients—joint sample "II".

Position	$\frac{de_i}{dT}$	EA $\frac{de_i}{dT}$	Position	$\frac{de_i}{dT}$	EA $\frac{de_i}{dT}$
	rad $\times 10^6/\mathrm{N}^{-1}$			rad $\times 10^6/\mathrm{N}^{-1}$	
P_1	0.0075	0.116	P_7	0.0075	0.116
P_2	0.0211	0.327	P_8	0.0162	0.251
P_3	0.0347	0.538	P_9	0.0249	0.386
Q_3	0.0362	0.562	Q_9	0.0259	0.401
Q_4	0.0348	0.539	Q_{10}	0.0265	0.411
P_4	0.0333	0.517	P_{10}	0.0253	0.392
P_5	0.0201	0.312	P_{11}	0.0109	0.170
P_6	0.0069	0.107	P_{12}	0.0034	0.053

As it is easy to understand, the strain analysis allows the estimation of the gradient of axial forces N' and N'' with respect to the equilibrium scheme of the joint (Figure 18). Moreover, the global gradient at the left cross-section Q_3–Q_9 ($dN'/dT + dN''/dT$) emerges substantially equal to the one attained at the right cross-section Q_4–Q_{10} ($dN'/dT + dN''/dT$) for both of the joint samples "I" and "II", thus indicating that equilibrium is satisfied with a quasi-balanced distribution of the axial forces between the external adherents "2" and "3". It is important to remark that strain gauges are applied to the top/bottom sides of the external adherents and are unable to account for possible shear deformations within the thickness of the GFRP, which, together with experimental minor errors, may be responsible for the following apparent paradoxes:

$$(a)\ dN'/dT + dN''/dT \neq 1$$

$$(b)\ dN'/dT\big|Q_3 \neq dN'/dT\big|Q_4$$

$$(c)\ dN''/dT\big|Q_9 \neq dN''/dT\big|Q_{10}$$

3.2. Numerical Results

In order to compare experimental results to the numerical ones, the experimental response of the joint samples has been reproduced via a numeric simulation according to many simplifications. In particular, the loading steps are simplified compared to those given in Tables 7 and 8 and are provided in Table 11.

Table 11. Multi-step testing procedure for numerical experiment.

Cycles			(*)	Target	
2, 3	(a)	loading	DC	+1.00	mm
	(b)	unloading	FC	0.00	N
Final		loading	DC	+ 1.30	mm

(*) DC: displacement control; FC: force control

Moreover, the mechanical properties of the materials are the following.

- GFRP adherents. The Young's modulus is equal to E = 37,000 N/mm^2 (which is approximatively the stiffness observed in the preliminary tests) and the Poisson's ratio $\upsilon = 0.2$.
- interfaces. The epoxy resin has a Young's modulus equal to E = 2000 N/mm^2 (according to Table 2), a Poisson's ratio equal to $\upsilon = 0.2$, the viscosities are equal to $\gamma = 0.008$, $\omega = -0.0001$ and the length of the representative elementary volume is equal to $L = 0.1$ mm. For the computation of the crack length, the time increment is set equal to $\Delta t = 0.01$ s.

The materials remain purely elastic with no failure criterion playing a role.

4. Discussion

Figures 19 and 20 give a comparison between the experimental and numerical results for the double-lap joint as depicted in Figures 1 and 2. In the following, a comparison between numerical results and both the main experiments is discussed.

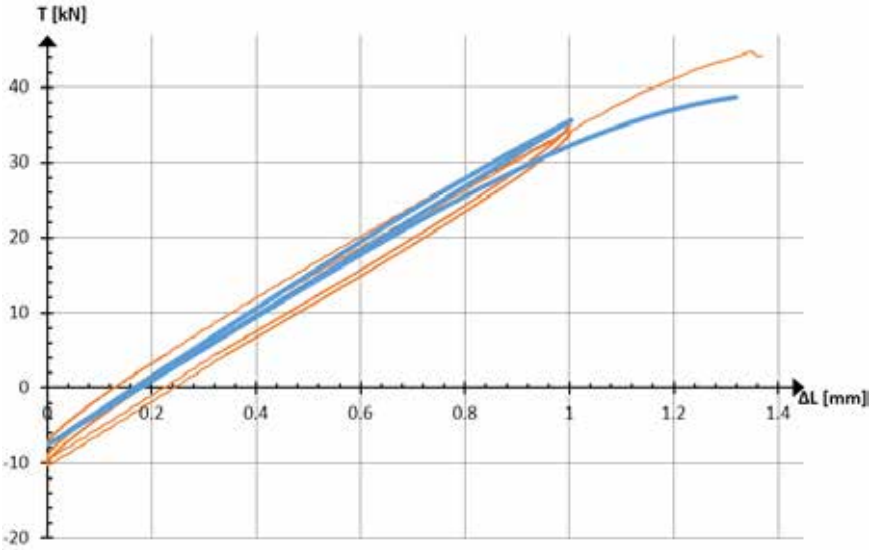

Figure 19. Numerical (**blue**) and experimental comparison for joint sample "I" (**orange**).

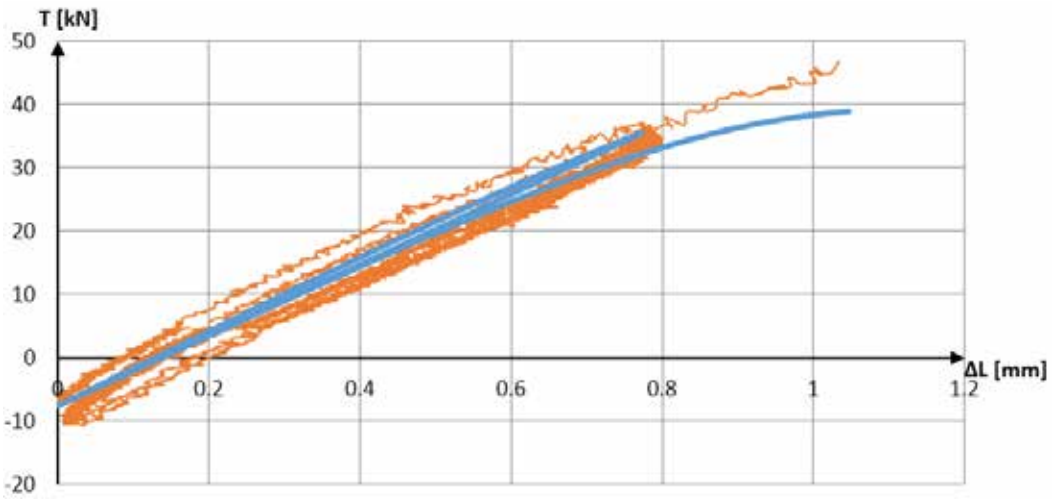

Figure 20. Numerical (**blue**) and experimental comparison for joint sample "II" (**orange**).

Experimental results show that the sample accommodates itself in a stable configuration after the first loading/unloading step; thus, it is assumed that the configuration attained at the end of the first unloading step is an origin for the further steps. It is observed that the numerical experiments are able to reproduce the two cycles "2" and "3" with a good agreement.

The blue curve for the numerical test, and the orange/red one for the experimental results, are close to each other. Moreover a similar hysteresis is observed. It is important that the theoretical model does not initially include a complete failure criterion; the failure is obtained only if the damage parameter is equal to infinity, and then it is not possible to reproduce the complete failure of the joint numerically. The model has been improved, introducing a complementary criterion (a large value of the damage parameter) in order to obtain the complete rupture of the interface.

In Figure 21 also presents the evolution of the damage variable l [mm] during the numerical experiment over cycles "2", "3", and over the final step. It is worthy of remarking that, in the proposed model, the damage variable is the averaged length l of the cracks in the interface, and it is always increasing. This property is also observed in Figure 21.

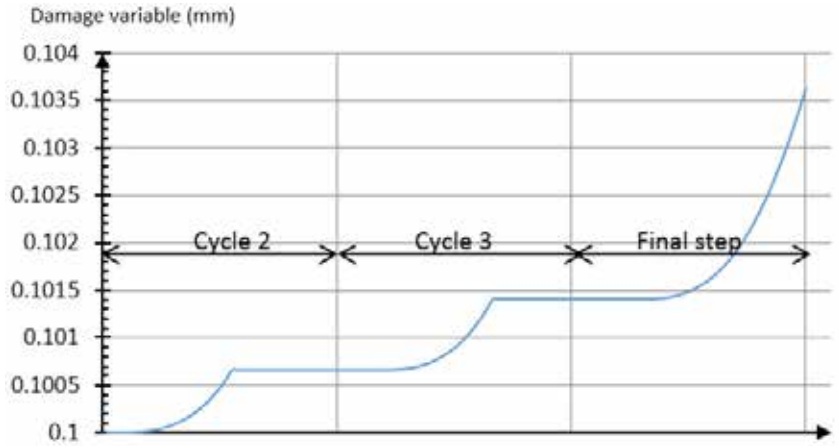

Figure 21. Evolution of the damage variable l [mm] over cycles "2", "3", and the final step.

5. Conclusions

In this paper, a study dealing with double lap joints made of GFRP material and an epoxy resin as a glue, under loading conditions that produce damage within the bonding interfaces is conducted and an experimental setup is presented. Both experiments and a theoretical model are proposed to

study the damage within FRP bonded joints. The theoretical model is implemented numerically. A comparison between experimental and theoretical results with the associated numerical procedure is proposed. The experimental and the numerical analyses are in a very good agreement. The results show that it is possible to associate an experimental procedure and a theoretical model in order to reproduce and predict the behaviour of FRP joints. In the future, we want to extend this preliminary study, accounting for many geometric configurations, and to improve the theoretical model considering failure criteria and friction, in order to perform the analysis of the post-failure behaviour, too.

Acknowledgments: ATP-Pultrusion S.r.l. and Kerakoll S.p.a. companies contributed to this research providing for free GFRP samples and the epoxy-resin, respectively. No other grant nor funds there were in support of the research.

Author Contributions: For this research, Agostina Orefice and Geminiano Mancusi designed and performed the experimental tests, while Serge Dumont and Frédéric Lebon developed the interface model and carried out the numerical simulations.

Conflicts of Interest: The authors declare no conflict of interest.

References

1. Hasegawa, K.; Crocombe, A.D.; Coppuck, F.; Jewell, D.; Maher, S. Characterising bonded joints with a thick and flexible adhesive layer-Part 1: Fracture testing and behaviour. *Int. J. Adhes. Adhes.* **2015**, *63*, 124–131. [CrossRef]
2. Hasegawa, K.; Crocombe, A.D.; Coppuck, F.; Jewell, D.; Maher, S. Characterising bonded joints with a thick and flexible adhesive layer-Part 2: Fracture testing and behaviour. *Int. J. Adhes. Adhes.* **2015**, *63*, 158–165. [CrossRef]
3. Chaves, F.J.P.; Da Silva, L.F.M.; De Moura, M.F.S.F.; Dillard, D.A.; Esteves, V.H.C. Fracture mechanics tests in adhesively bonded joints: A literature review. *J. Adhes.* **2014**, *90*, 955–992. [CrossRef]
4. Rodríguez, R.Q.; De Paiva, W.P.; Sollero, P.; Rodrigues, M.R.B.; De Albuquerque, É.L. Failure criteria for adhesively bonded joints. *Int. J. Adhes. Adhes.* **2012**, *37*, 26–36. [CrossRef]
5. Narayanamurthy, V.; Chen, J.F.; Cairns, J. Improved model for interfacial stresses accounting for the effect of shear deformation in plated beams. *Int. J. Adhes. Adhes.* **2016**, *64*, 33–47. [CrossRef]
6. Mancusi, G.; Ascione, F. Performance at collapse of adhesive bonding. *Compos. Struct.* **2013**, *96*, 256–261. [CrossRef]
7. Li, J.; Yan, Y.; Zhang, T.; Liang, Z. Experimental study of adhesively bonded CFRP joints subjected to tensile loads. *Int. J. Adhes. Adhes.* **2015**, *57*, 95–104. [CrossRef]
8. Feo, L.; Mancusi, G. Modeling shear deformability of thin-walled composite beams with open cross-section. *Mech. Res. Commun.* **2010**, *37*, 320–325. [CrossRef]
9. Feo, L.; Mancusi, G. The influence of the shear deformations on the local stress state of pultruded composite profiles. *Mech. Res. Commun.* **2012**, *47*, 44–49. [CrossRef]
10. Mancusi, G.; Feo, L. Non-linear pre-buckling behavior of shear deformable thin-walled composite beams with open cross-section. *Compos. B Eng.* **2013**, *47*, 379–390. [CrossRef]
11. Mancusi, G.; Ascione, F.; Lamberti, M. Pre-buckling behavior of composite beams: A mechanical innovative approach. *Compos. Struct.* **2014**, *117*, 396–410. [CrossRef]
12. Costa, I.; Barros, J. Tensile creep of a structural epoxy adhesive: Experimental and analytical characterization. *Int. J. Adhes. Adhes.* **2015**, *59*, 115–124. [CrossRef]
13. Puigvert, F.; Crocombe, A.D.; Gil, L. Fatigue and creep analyses of adhesively bonded anchorages for CFRP tendons. *Int. J. Adhes. Adhes.* **2014**, *54*, 143–154. [CrossRef]
14. Mancusi, G.; Spadea, S.; Berardi, V.P. Experimental analysis on the time-dependent bonding of FRP laminates under sustained loads. *Compos. B Eng.* **2013**, *46*, 116–122. [CrossRef]
15. Marante, M.E.; Flórez-López, J. Three-Dimensional analysis of reinforced concrete frames based on lumped damage mechanics. *Int. J. Solids Struct.* **2003**, *40*, 5109–5123. [CrossRef]
16. Amorim, D.L.D.F.; Sergio, P.B.; Proença, S.P.B.; Flórez-López, J. A model of fracture in reinforced concrete arches based on lumped damage mechanics. *Int. J. Solids Struct.* **2013**, *50*, 4070–4079. [CrossRef]
17. Bonetti, E.; Bonfanti, G.; Lebon, F.; Rizzoni, R. A model of imperfect interface with damage. *Meccanica* **2016**, accepted.

18. Mauge, C.; Kachanov, M. Effective elastic properties of an anisotropic material with arbitrarily oriented interacting cracks. *J. Mech. Phys. Solids* **1994**, *42*, 561–584. [CrossRef]
19. Tsukrov, I.; Kachanov, M. Effective moduli of an anisotropic material with ellipticalholes of arbitrary orientational distribution. *Int. J. Solids Struct.* **2000**, *37*, 5919–5941. [CrossRef]
20. Klarbring, A. Derivation of the adhesively bonded joints by the asymptotic expansion method. *Int. J. Eng. Sci.* **1991**, *29*, 493–512. [CrossRef]
21. Lebon, F.; OuldKhaoua, A.; Licht, C. Numerical study of soft adhesively bonded joints in finite elasticity. *Comput. Mech.* **1998**, *21*, 134–140. [CrossRef]
22. Rekik, A.; Lebon, F. Identification of the representative crack length evolution in amulti-level interface model for quasi-brittle masonry. *Int. J. Solids Struct.* **2010**, *47*, 3011–3021. [CrossRef]
23. Rekik, A.; Lebon, F. Homogenization methods for interface modeling in damaged masonry. *Adv. Eng. Softw.* **2012**, *46*, 35–42. [CrossRef]
24. Dumont, S.; Lebon, F.; Rizzoni, R. An asymptotic approach to the adhesion of thin stiff films. *Mech. Res. Commun.* **2014**, *58*, 24–35. [CrossRef]
25. Frémond, M. Adhérence des solides. *J. Mec. Théor. Appl.* **1987**, *6*, 383–407. (In French)
26. Fouchal, F.; Lebon, F.; Raffa, M.L.; Vairo, G. An interface model including cracks and roughness applied to masonry. *Open Civ. Eng. J.* **2014**, *8*, 263–271. [CrossRef]
27. Dumont, S.; Lebon, F.; Raffa, M.L.; Rizzoni, R.; Welemane, H. Multiscale modeling of imperfect interfaces and applications. In *Computational Methods in Applied Sciences*; Springer: Berlin/Heidelberg, Germany, 2016; Volume 41, pp. 81–122.
28. Raffa, M.L. Micromechanical Modeling of Imperfect Interfaces and Applications. Ph.D. Thesis, University of Rome Tor Vergata, Rome, Italy, 2015.
29. Nairn, J.A. Numerical implementation of imperfect interfaces. *Comput. Mater. Sci.* **2007**, *40*, 525–536. [CrossRef]